Shape Transition and Propulsive Force of an Elastic Rod Rotating in a Viscous Fluid

Bian Qian, Thomas R. Powers, and Kenneth S. Breuer*

Division of Engineering, Box D, Brown University, Providence, Rhode Island 02912, USA

(Received 2 December 2007; published 19 February 2008)

The deformation of an elastic rod rotating in a viscous fluid is considered, with applications related to flagellar motility. The rod is tilted relative to the rotation axis, and experiments and theory are used to study the shape transition when driven either at constant torque or at constant speed. At low applied torque, the rod bends gently and generates small propulsive force. At a critical torque, the rotation speed increases abruptly, and the rod forms a helical shape with increased propulsive force. We find good agreement between theory and experiment. A simple physical model is presented to capture and explain the essential behavior.

DOI: 10.1103/PhysRevLett.100.078101 PACS numbers: 87.16.Qp, 46.70.Hg, 47.15.G−

Understanding how flagella and cilia work is a central aim of the field of cell motility. The problem may be split into two parts: the means of actuation and the fluid-structure interaction. In this Letter, we consider the fluid-structure interaction for thin filaments in a viscous fluid. At micron scales, viscous effects dominate inertia, and the fluid-structure interaction problem simplifies because the Stokes equations governing the fluid motion are linear. Gray and Hancock used this linearity to develop a simple theory that successfully predicted the swimming speed of a sperm cell with a load-independent pattern of bending waves propagating along the flagellum [1]. Soon after, Machin considered the fluid-structure interaction [2]. He argued that the motors must be distributed along the length of the flagellum, since, for small amplitudes, a passive flexible rod waved at one end has an exponentially decaying envelop of deflection, whereas the amplitude of deflection in real flagellar bending waves increases slightly with distance from the head [2]. The shapes and propulsive forces of a passive rod actuated at one end have recently been examined theoretically [3,4] and experimentally [4]. Although sperm flagella are not passive, the results of [2–4] are important for modeling real flagella since the modes that Machin found also enter models in which the flagellum is actuated along its entire length [5].

Rotating flagella are also common. For example, nodal cilia [6] have an internal structure similar to that of sperm flagella. However, instead of beating in a plane like most sperm flagella, nodal cilia rotate along the surface of an imaginary cone. The flow set up by these flagella has been implicated in the formation of left-right asymmetry in developing embryos (see [6] and references therein). Bacterial flagella provide another example. These flagella are helical, much thinner than eukaryotic flagella, and driven by a rotary motor embedded in the cell wall. Fluid-structure interactions are important for polymorphic transformations in swimming bacteria [7] and the bundling of multiple flagella [8].

Complementary to the problem of understanding how biological flagella work is the problem of building an artificial microscopic flagellum-propelled swimmer, recently demonstrated by Dreyfus *et al.* [9], who used a rotating external magnetic field to generate propagating planar bending waves in a filament composed of a string of colloidal magnetic particles. A challenge in building an artificial microscopic swimmer is the means of actuation. Manghi *et al.* proposed a mechanism in which a microscopic flexible rod rotates along the surface of an imaginary cone [10,11]. Using numerical methods, they predicted that at a critical driving torque, the rod will undergo a discontinuous transition to a helical shape with significant propulsive force, independent of the sense of rotation. In this Letter, we present a macroscopic experimental realization of this system, as well as new theoretical results that complement previous hydrodynamic calculations [10,11]. In addition, we present a simple physical model which captures the essential physics, and helps in the interpretation of the observed behavior.

In our experiment, a servo motor rotates a flexible rod in highly viscous silicone oil. The rod is connected to the motor shaft such that the base of the rod makes a fixed angle with the rotation axis [Fig. 1(a)]. The motor may be operated either at constant speed or at constant torque. The range of torques explored was 0.5 to 8 mN m, and the maximum rotation frequency was less than 0.3 Hz. The rod is a steel extension spring wrapped in Teflon™ tape; the tape stiffens the rod to minimize sagging. The diameter of the rod is $a = 2.5$ mm, and the bending modulus is $A \approx 3 \times 10^{-3}$ N/m^2. Rod lengths L from 210 to 290 mm were tested. The silicone oil has viscosity $\eta \approx 110$ N m^2/s and is held in a tank 420 mm on each side. With these parameters, the Reynolds number $\mathrm{Re} = \rho v L/\eta \approx 10^{-1}$, where $\rho \approx 10^3$ kg/m^3 is the fluid density, $v \approx 10^{-1}$ m/s is the typical velocity of the free end of the rod, and $L \approx 10^{-1}$ m. Front and side images of the steady-state three-dimensional shape of the rotating rod at each torque were captured using a single camera and a single mirror. The imaging system was carefully calibrated to account for perspective, achieving an accuracy of ± 2 mm.

At low torque, the rotation speed is relatively slow, and the rod bends slightly [Fig. 1(a)]. Above a critical torque, the rod adopts a helical shape and rotates much faster

 © 2008 The American Physical Society

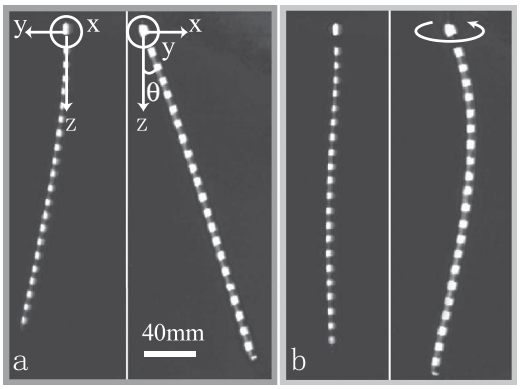

FIG. 1. Orthogonal images of steady-state shapes of rotating rod with torque just below (a) and just above (b) the critical torque. The motor (not shown) is at the top, with rotation axis along z. Gravity points down. In (a) and (b), the left panel is the side view, and the right panel is the front view. The rod is marked with white dots for contrast. The axes in (b) are the same as in (a). The curved arrow in (b) denotes the sense of rotation of the rod.

[Fig. 1(b)]. To illustrate the physics, we first present a simple analysis of this shape transition using the lumped parameter model shown in Fig. 2. The rod is modeled by two rigid links of unit length connected by a torsional spring. The link OP is fixed at angle θ between the rotation axis $\hat{\mathbf{z}}$ and the base of the rod in our experiment. Since the Reynolds number is small, we take $\mathrm{Re} = 0$. Thus, we may work in the rod's rotating rest frame without introducing fictitious forces. The flow in this frame at point $\mathbf{r}$ is $\omega\hat{\mathbf{z}} \times \mathbf{r}$. The torsional spring represents the bending resistance and is only sensitive to changes in the angle between the vectors OP and PQ. Assuming $\theta \ll 1$ and K is sufficiently large, the moment about P on PQ from the spring is $M_b \approx K(OP \times PQ) \approx K(y, 2\theta - x, 0)$, where K is the torsional spring constant, and $(x, y, 2) \approx \mathbf{r}_Q$ is the position of the point Q to leading order in θ. To find the steady-state position of Q, equate the moment on PQ due to the torsional spring to the moment on PQ due to the flow. Assuming all drag on PQ is concentrated at Q (Fig. 2), the viscous moment about P is $M_v \approx -\zeta\omega(x, y, 0)$, where ζ is a resistance coefficient. Solving moment balance for x and y yields $x = 2\theta/[1 + (\zeta\omega/K)^2]$ and $y = x\zeta\omega/K$. As

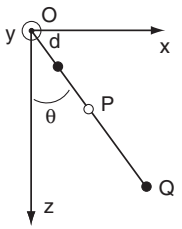

FIG. 2. Lumped parameter model consisting of two rigid links connected by a torsional spring (open circle). The top link is clamped. All drag is concentrated at the two filled circles.

ω increases from zero, the link PQ deflects and y increases, which causes Q to experience a viscous force in the negative x direction. These forces push Q toward the rotation axis, and tend to cause the rod in our experiment to wrap around the z axis. As ω increases further, Q moves closer to the rotation axis, and y begins to decrease. There is also some drag on the link OP, concentrated a distance d from O. The moment about O due to flow is

$$M_O = \zeta\omega\theta^2\left(d^2 + \frac{4}{1 + \zeta^2\omega^2/K^2}\right). \tag{1}$$

For $d^2 < 1/2$, we find that the moment first increases with ω, then decreases as the link folds in toward the rotation axis where the flow is slow. The moment then increases again as the drag from the base link OP dominates. If M_O is plotted vs ω, then we find an S-shaped curve, just as in our experiment (Fig. 3), with discontinuous transitions in shape and speed as moment varies.

We now turn to a more complete quantitative analysis. We will continue to prescribe ω rather than motor torque M_m, and we limit the analysis to steady-state shapes. Unlike Manghi *et al.* [10,11], we disregard hydrodynamic interactions between distant parts of the rod and use resistive force theory to model the force per unit length $\mathbf{f}$ acting on the rod [1,12]:

$$\mathbf{f} = \zeta_\perp(\mathbf{v} - \mathbf{r}_s\mathbf{r}_s \cdot \mathbf{v}) + \zeta_\parallel\mathbf{r}_s\mathbf{r}_s \cdot \mathbf{v}, \tag{2}$$

where $\zeta_\perp = 4\pi\eta/[\log(L/a) + 1/2]$ and $\zeta_\parallel = 2\pi\eta/[\log(L/a) - 1/2] \approx \zeta_\perp/2$, $\mathbf{r}(s, t)$ is the position of the point on the rod center line with arclength s at time t, $\mathbf{v}(s, t)$ is the velocity of the undisturbed flow relative to the velocity of the rod at s, and $\mathbf{r}_s = \partial\mathbf{r}/\partial s$ is the tangent vector to the rod center line. There is also a hydrodynamic

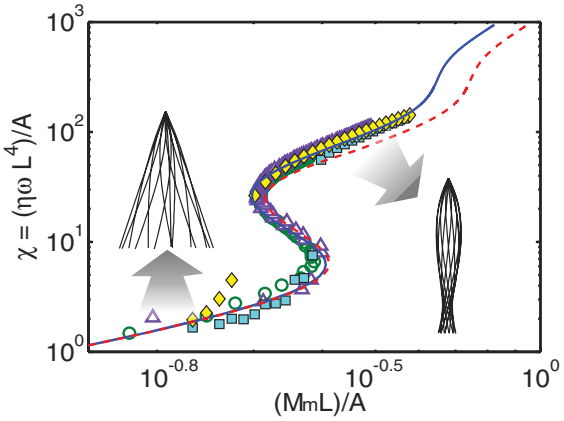

FIG. 3 (color online). Dimensionless motor torque M_mL/A was measured as a function of dimensionless speed χ for $L =$ 250 mm (○) and $L = 290$ mm (△) with angle $\theta = 26°$. For $L = 250$ mm, speed was measured as a function of increasing torque (■) and decreasing torque (◆). Note the hysteresis. The linear (dashed line) and nonlinear (solid line) predictions are shown. The insets show examples of the steady-state filament shapes in the low (left) and high (right) speed regimes.

torque distributed along the rod which induces twist [13–15]. However, the effects of this torque are smaller by a factor of $(a/L)^2$ relative to effects due to translation of the rod [13] and will henceforth be disregarded. The constitutive relation for the elastic rod is

$$\mathbf{M} = A\mathbf{r}_s \times \mathbf{r}_{ss}, \tag{3}$$

where $\mathbf{M}$ is the moment due to internal stresses exerted on the cross section of the rod at s, and A is the bending modulus [16]. The shape of the rod is determined by force and moment balance,

$$\mathbf{F}_s + \mathbf{f} + \mathbf{f}_g = \mathbf{0} \tag{4}$$

$$\mathbf{M}_s + \mathbf{r}_s \times \mathbf{F} = \mathbf{0}, \tag{5}$$

where $\mathbf{F}$ is the force due to internal stresses acting on the rod cross section at s, $\mathbf{F}_s = \partial\mathbf{F}/\partial s$, and $\mathbf{f}_g = (\mu_{\text{rod}} - \pi a^2 \rho_{\text{oil}}) g\hat{\mathbf{z}}$ is the buoyancy force per unit length due to the density difference between the rod (linear density $\mu_{\text{rod}} = 0.0478$ kg/m with oil inside) and silicone oil ($\rho_{\text{oil}} = 970$ kg/m^3). The boundary conditions are $\mathbf{r}(0) = \mathbf{0}$, $\mathbf{r}_s(0) = \hat{\mathbf{x}}\sin\theta + \hat{\mathbf{z}}\cos\theta$, $\mathbf{F}(L) = \mathbf{0}$, and $\mathbf{M}(L) = \mathbf{0}$ [16]. As in the lumped parameter model, $\mathbf{v} = \omega\hat{\mathbf{z}} \times \mathbf{r}$ at steady state in the rod frame.

The primary dimensionless groups governing the rod shape are the angle θ and the dimensionless rotation speed $\chi = \eta\omega L^4/A = (L/\ell)^4$, where $\ell = [A/(\eta\omega)]^{1/4}$ is the characteristic length scale determined by bending resistance and viscous drag [2,3]. In addition, the aspect ratio L/a and the nondimensional gravitational force $g\mu_{\text{rod}}L^3/A$ are included in the analysis, but not parametrically explored since they play a minor role. Figure 3 shows that experimental measurements, using two rod lengths, collapse well onto a single curve when dimensionless speed, χ, is plotted against dimensionless motor torque, $M_m L/A$. The open symbols represent constant velocity rotation and trace out the entire S-shaped curve. The filament shape is stable at every prescribed value of χ, and the shape changes continuously from the slightly bent shape to a helical shape as χ increases. The closed symbols represent constant torque operation. When driven at constant torque, there is a discontinuity in rotation speed and filament shape at two different torque values, depending if torque is ascending or descending. For descending torque, the time to reach steady state is prohibitively long, and the diamond symbols lying above the curve in Fig. 3 represent shapes that are relaxing slowly to steady state.

The nonlinear behavior of the speed-torque curve displayed in Fig. 3 can be qualitatively explained using linear approximations valid for small rod deflections. For small θ, the rod is aligned mainly along the z-axis and, disregarding gravity, the deflection $\mathbf{r}_\perp(z) = (x(z), y(z))$ obeys

$$-A\frac{\partial^4 \mathbf{r}_\perp}{\partial z^4} + \zeta_\perp \omega\hat{\mathbf{z}} \times \mathbf{r}_\perp = \mathbf{0}. \quad -\ell^4\frac{\partial^4 \mathbf{r}_\perp}{\partial z^4} + \hat{\mathbf{z}} \times \mathbf{r}_\perp = \mathbf{0}. \tag{6}$$

The solution to Eq. (6) is a generalization of Machin's solution to the in-plane bending problem [2], and of the same form as the solution for a flexible rod held parallel to but some distance from the axis of rotation [17].

To calculate the torque M_m required to rotate the rod at speed ω, observe that the moment due to viscous drag must equal the elastic moment at the base of the rod:

$$M_m = -\hat{\mathbf{z}} \cdot \int \mathbf{r} \times \mathbf{f} ds = -A\hat{\mathbf{z}} \cdot \mathbf{r}_s \times \mathbf{r}_{ss}(0). \tag{7}$$

The second equality of (7) follows from (4) and (5). The results of the linear calculation for driving torque vs speed are shown in Fig. 3 along with the experimental data for $\theta = 26°$. For small χ, M_m increases linearly with χ. For large χ, Eq. (6) implies that the shape of the rod is helical with an envelope that decays exponentially with length scale ℓ. Assuming isotropy $x \sim y$ and using force balance (6), the viscous force per length $f \sim \eta\omega y \sim Ay/\ell^4$, which implies a total viscous moment $M_v L/A \sim Ly^2/\ell^3$. On the other hand, the bending moment at the base of the rod scales as $M_b L/A \sim yL/\ell^2$. Equating M_v and M_b yields $y \sim \ell = L\chi^{-1/4}$ [18]. Thus, for $\chi \gg 1$, the motor torque must scale as $M_m L/A \sim \chi^{1/4}$. Unfortunately, our experiment cannot access this high-speed regime due to limitations in the torque-speed characteristic of our motor. We also observe an intermediate scaling, $M_m L/A \sim \chi^{1/2}$. This

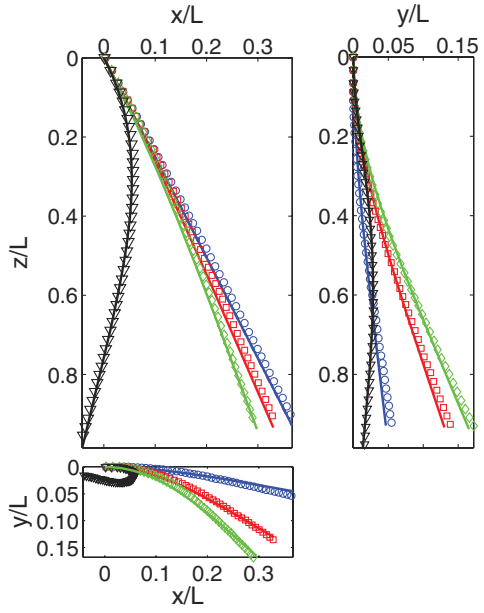

FIG. 4 (color online). Steady-state shapes of a rotating rod from experimental measurements for $\chi = 1.38$ (○), 4.25 (□), 5.91 (◇) (before transition), and 164.63 (▽) (after transition), along with the shapes calculated from the nonlinear (solid line) theory. The rod has $L = 210$ mm and $\theta = 20°$.

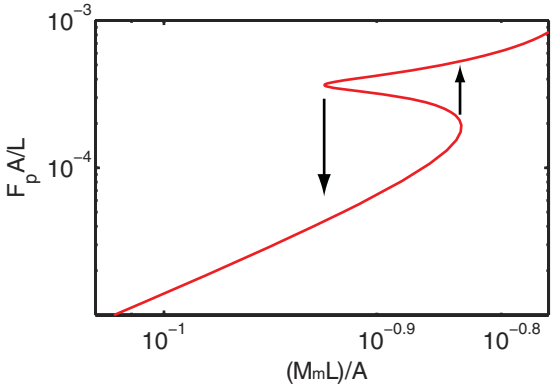

FIG. 5 (color online). Theoretical calculation of the dimensionless propulsion force F_p as a function of dimensionless M_m for $\theta = 20°$, using the nonlinear equations for the ideal case of zero gravity. The arrows denote the transition for ascending (↑) and descending (↓) torque.

scaling arises since in this subasymptotic regime, the deflection $y \sim L\chi^{-1/4}$, but the scale for bending of the rod is still L and not ℓ.

For large θ, the deflection of the rod is significant even for small χ, and the linear theory is inaccurate. However, the nonlinear Eqs. (2)–(5) are readily solved with shooting methods [19]. The nonlinear theory gives a more accurate prediction for the speed-torque relationship in the high-speed regime where the linear and nonlinear theories differ (Fig. 3). As θ increases, the general appearance of the torque-speed relationship remains unchanged although both the critical torque and the jump in speed at the transition increase (not shown here). Finally, for large χ, the linear scaling analysis presented above remains valid, and the moment scales like $\chi^{1/4}$ for $\chi \gg 1$.

Figure 4 shows the steady-state rod shapes for four different values of χ, comparing experimental data (symbols) with the nonlinear theory (solid line). The agreement between theory and experiment is good. Note that the y-z projection shows how $y(L)$ first increases with χ and then decreases, in accord with our intuitive argument.

We can calculate the thrust, or axial force, from the shape of the rod using $F_p = \hat{\mathbf{z}} \cdot \int \mathbf{f} ds = -\hat{\mathbf{z}} \cdot \mathbf{F}(0)$. The kinematic reversibility of Stokes flow implies that a rigid rod rotating along the surface of a cone generates zero propulsive thrust. For small χ, the elastic rod deforms slightly and generates little thrust. Above the critical torque, as the helical shape develops, the thrust increases abruptly (Fig. 5). Since the shape of an actuated elastic filament cannot be decoupled from swimming kinematics [20], it would be an interesting generalization of our work to build an artificial swimmer driven by a rotating elastic rod, tilted at the base to the rotation axis.

This work was supported in part by National Science Foundation Grants Nos. CTS-0508349 (K. S. B.), NIRT-0404031 (T. R. P.), and DMS-0615919 (T. R. P.). As we were completing this Letter, we learned of the work of the group of Fermigier, who have conducted a similar experiment [21].

*kbreuer@brown.edu

[1] J. Gray and G. J. Hancock, J. Exp. Biol. **32**, 802 (1955).
[2] K. Machin, J. Exp. Biol. **35**, 796 (1958).
[3] C. H. Wiggins and R. E. Goldstein, Phys. Rev. Lett. **80**, 3879 (1998).
[4] T. S. Yu, E. Lauga, and A. E. Hosoi, Phys. Fluids **18**, 091701 (2006).
[5] S. Camalet, F. Jülicher, and J. Prost, Phys. Rev. Lett. **82**, 1590 (1999).
[6] H. A. Praetorius and K. R. Spring, Annual Review of Physiology **67**, 515 (2005).
[7] L. Turner, W. Ryu, and H. Berg, J. Bacteriol. **182**, 2793 (2000).
[8] M. J. Kim, J. C. Bird, A. J. Van Parys, K. S. Breuer, and T. R. Powers, Proc. Natl. Acad. Sci. U.S.A. 100, 15481 (2003).
[9] R. Dreyfus, J. Baudry, M. L. Roper, M. Fermigier, H. A. Stone, and J. Bibette, Nature (London) **437**, 862 (2005).
[10] M. Manghi, X. Schlagberger, and R. R. Netz, Phys. Rev. Lett. **96**, 068101 (2006).
[11] M. Manghi, X. Schlagberger, Y.-W. Kim, and R. R. Netz, Soft Matter **2**, 653 (2006).
[12] J. B. Keller and S. I. Rubinow, J. Fluid Mech. **75**, 705 (1976).
[13] C. W. Wolgemuth, T. R. Powers, and R. E. Goldstein, Phys. Rev. Lett. **84**, 1623 (2000).
[14] S. Lim and C. S. Peskin, SIAM J. Sci. Comput. **25**, 2066 (2004).
[15] H. Wada and R. R. Netz, Europhys. Lett. **75**, 645 (2006).
[16] L. D. Landau and E. M. Lifshitz, *Theory of Elasticity* (Pergamon Press, Oxford, 1986), 3rd ed..
[17] T. R. Powers, Phys. Rev. E **65**, 040903 (2002).
[18] S. A. Koehler and T. R. Powers, Phys. Rev. Lett. **85**, 4827 (2000).
[19] W. H. Press, W. T. Vetterling, S. A. Teukolsky, and B. P. Flannery, *Numerical Recipes in C* (Cambridge University Press, Cambridge, England, 1992), 2nd ed..
[20] E. Lauga, Phys. Rev. E **75**, 041916 (2007).
[21] M. Fermigier, N. Champagne, E. Laik, J. Marthelot, and O. du Roure, "Rotational Dynamics of a Soft Filament: Wrapping Transition and Propulsive Forces" (to be published).